Baroclinic Eady Wave and Fronts. Part I: Viscous Semigeostrophy and the Impact of Boundary Condition

QIN XU

Naval Research Laboratory, Monterey, California

WEI GU

Department of Atmospheric Sciences, Nanjing University, Nanjing, China, and CIMMS, University of Oklahoma, Norman, Oklahoma

JIDONG GAO

CAPS, University of Oklahoma, Norman, Oklahoma

(Manuscript received 21 April 1997, in final form 16 March 1998)

ABSTRACT

A two-dimensional viscous semigeostrophic model is developed to study the evolution of the baroclinic Eady wave and fronts with two types (free-slip and nonslip) of boundary conditions. With the free-slip boundary condition, the solution is very similar to the inviscid one but the frontal collapse is prevented by the diffusive effect. When the fronts become sharp in the mature stage, strong horizontal diffusions of momentum and potential temperature cause strong inward fluxes of geostrophic potential vorticity (GPV) at the surface fronts, so high GPV anomalies are generated at the surface fronts and advected into the interior, forming two backward-tilted plumes along the upper and lower fronts. The wave and front development can be interpreted by the interaction between the lower- and upper-level GPV anomalies in terms of GPV thinking similarly to that in the inviscid case.

When the boundary condition is nonslip, the initial growth and subsequent nonlinear evolution of the solution are significantly slower than the inviscid one, but the associated boundary layer processes allow the model to produce realistic features in the vicinity of the front. Diffusive GPV fluxes at the boundaries are caused mainly by vertical diffusions of momentum and potential temperature, so GPV anomalies are produced over broad regions behind and ahead of the front. As the GPV anomalies are transported from the boundary layer into the interior, they evolve into two mushroom clouds. The shallow boundary layer circulation, driven by the inverted geostrophic flow through Ekman pumping, produces a positive feedback to the horizontal spreading of the interior GPV anomalies. This explains why and how the GPV anomalies grow into two mushroom clouds.

1. Introduction

In the inviscid semigeostrophic (SG) Eady wave model (Hoskins and Bretherton 1972), the upper and lower boundaries can be viewed as two reservoirs of geostrophic potential vorticity (GPV) in which isentropic layers of infinitesimal thickness are packed, and surface potential temperature anomaly can be viewed as delta-function GPV anomalies at the boundaries (Bretherton 1966). The interior GPV maintains its constant value before the surface front collapses (Hoskins and Bretherton 1972). After the surface front collapses, the isentropic surfaces in the boundary GPV reservoir are folded into the interior fluid, and delta-function GPV anomalies intrude from their reservoirs into the interior fluid (Cullen and Purser 1984; Purser and Cullen 1987; Cho and Koshyk 1989; Koshyk and Cho 1992, also see Fig. 1 of this paper). Thus, there are two distinctly different stages for the growth of GPV anomalies in the inviscid Eady wave: (i) the boundary stage and (ii) the interior stage. The boundary stage occurs before the surface fronts collapse. During this stage the GPV anomalies are generated only at the boundaries in the forms of delta functions associated with the surface potential temperature anomalies. The interior stage occurs after the surface fronts collapse. During this second stage, strong (delta function) GPV anomalies intrude into the interior fluid from the boundary GPV reservoirs. The interaction between the upper- and lower-level GPV

Corresponding author's address: Dr. Qin Xu, Naval Research Laboratory, Monterey, CA 93943-5502.
E-mail: xuq@nrlmry.navy.mil

© 1998 American Meteorological Society

Unauthenticated | Downloaded 08/04/24 02:39 AM UTC

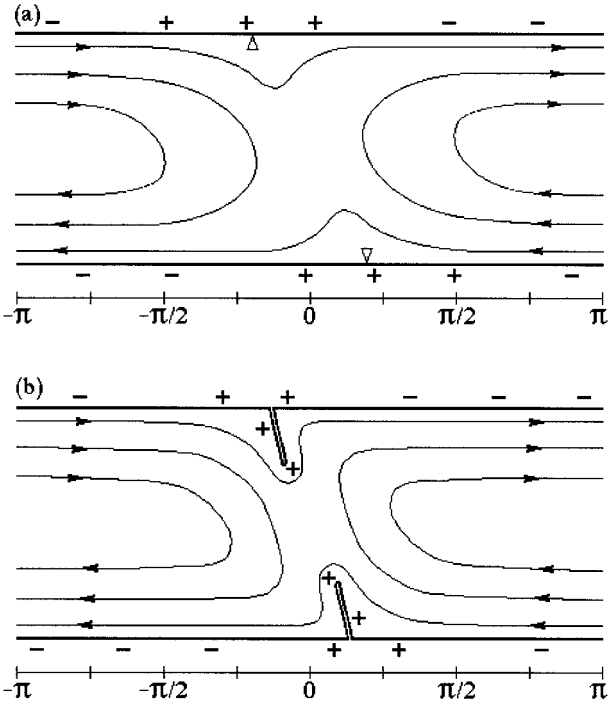

FIG. 1. Sketches of the distribution of surface potential temperature anomalies during the boundary stage (a) and interior stage (b). Surface potential temperature anomalies are represented by ''surface charges'' of delta-function GPV anomalies: + for positive and − for negative. Cross-front flows are shown by streamlines and arrows. Horizontal coordinate is plotted for one wavelength (from $-\pi$ to π). Surface fronts are indicated by hollow triangles in (a). As shown in (b) for the interior stage, ''surface charges'' are further enhanced (by the alongfront temperature advection) and moved (by the cross-front flow convergence) into the interior fluid along the folded surface on the two sides of each internal front.

anomalies and related wave dynamics in these two stages can be reviewed as follows.

During the boundary stage, there is no interior GPV anomaly, and the perturbation flow field is completely determined by the delta-function GPV anomalies at the boundaries. By viewing the delta-function GPV anomalies as the surface charges of a problem in electrostatics with the geopotential playing the role of the electric potential, the wave dynamics can be interpreted in terms of interaction of GPV anomalies between the upper and lower boundary; that is, the geostrophic flow induced by the delta-function GPV anomaly at each boundary ''keeps the other in step and makes the other grow'' [see Eq. (69) of Hoskins et al. 1985]. This interpretation or, say, ''GPV thinking'' is clean and accurate for the inviscid Eady wave problem formulated in the SG space using the geostrophic coordinate transformation [see Eq. (11) of Hoskins 1975]. By recovering the ageostrophic displacement, the SG space is transformed to physical space and the surface potential temperature anomaly is compressed (expanded) in the area of low (high) surface pressure where the ageostrophic wind converges (diverges) (Hoskins and Bretherton 1972; Xu 1988, 1990). As sketched in Fig. 1a, the surface front is formed in the area of positive GPV anomaly (represented by positive ''surface charge'') where the horizontal ageostrophic flow is strongly convergent. The ageostrophic displacement causes the horizontal distance between the upper and lower fronts to become shorter than a quarter wavelength in physical space.

The interior stage begins after discontinuities of potential temperature are produced at the boundaries and the discontinuities further intrude into the interior fluid. As sketched in Fig. 1b, surface potential temperature anomalies (represented by ''surface charges'') are further enhanced (by the along-front temperature advection) and moved (by the cross-front flow convergence) into the interior fluid along the folded surface on the two sides of each internal front. The internal front acts like a materiel surface separating the fluid on its two sides. As the two internal fronts grow into the interior fluid, they shift horizontally toward each other and the interaction between the upper and lower ''surface charges'' (delta-function GPV anomalies) is enhanced locally. The development of internal fronts can also be interpreted in terms of GPV thinking except that the upper and lower ''surface charges'' in the SG space are no longer on flat boundaries as the internal fronts in physical space are transformed into growing ''domes'' in the SG space (Purser and Cullen 1987; Koshyk and Cho 1992).

Intrusions of boundary GPV anomalies are essential features of the nonlinear dynamics of mature fronts, and the frontal discontinuity predicted by the inviscid SG theory is subject to turbulent diffusion in the real atmosphere or to parameterized turbulent diffusion (including numerical diffusion) in a numerical model of the atmosphere. Intrusions of boundary GPV anomalies, together with turbulent diffusion, play an important role in modifying the interior GPV structure and regulating the nonlinear evolution of the fronts and baroclinic waves. The related problems were examined by Nakamura and Held (1989) using a primitive equation model and by Nakamura (1994) using a viscous SG model for two-dimensional Eady waves. Their results showed that GPV anomalies created diffusively at the surface fronts played a pivotal role in the wave amplitude saturation and long-term evolution of the equilibrated flow, and the postsaturation dynamics depended sensitively on the specific forms of diffusion. It was also shown by Nakamura (1994) that the viscous SG model was able to reproduce the large-scale features of the solution of the primitive equation model very well, the difference of the two solutions largely represented the signal of high-frequency transients in the form of inertial-gravity waves emanating from the surface fronts, and the feedback of inertial-gravity waves on the large-scale dynamics were negligible. These results suggest that a viscous SG models can be very useful in studies of the

Unauthenticated | Downloaded 08/04/24 02:39 AM UTC

balanced dynamics of frontogenesis and evolution of baroclinic instability in two dimensions.

In the aforementioned studies, only one type of free-slip boundary condition was used with an ad hoc assumption that the nonflux condition applied only to the ageostrophic flow. It is not clear how the creation of GPV anomalies at the surface fronts should be affected by different boundary conditions. Since GPV anomalies are created diffusively at the surface fronts, different boundary conditions may produce very different patterns of GPV anomalies at the surface fronts and thus cause the fronts and baroclinic instability to evolve very differently. To study these problems, the viscous SG model of Xu (1989, 1992) will be extended in this paper and used to simulate the evolution of Eady baroclinic waves and fronts with two types of boundary conditions: free-slip and nonslip boundary conditions. Since these two boundary conditions are derived from the variational principle (Xu 1992) and apply to the total perturbation flow, they are admissible both mathematically and physically. Intrusions of GPV anomalies at the surface fronts have been interpreted in terms of pinching-off isentropes from high GPV reservoirs at the boundaries (Nakamura and Held 1989) and in terms of ''roll-up'' mechanism (Garner et al. 1992). The detailed distributions of GPV fluxes, however, could be complex in the vicinities of surface fronts and sensitive to boundary conditions. The related problems will be also examined in this paper.

A nonslip boundary condition with parameterized turbulent eddy viscosity was used by Cooper et al. (1992) in their nonhydrostatic Boussinesq model to examine the role of diffusive effects on potential vorticity (PV) in a two-dimensional Eady wave. As their analysis was focused mainly on the generation of the interior Rossby-Ertel PV anomalies within the boundary layer, they did not address the specific problems concerned in this study regarding (i) how the ''surface charges'' are affected by the diffusive processes with different boundary conditions, (ii) how the GPV fluxes are generated diffusively at the boundary and transport the GPV anomalies into the boundary layer and further into the interior atmosphere above the boundary layer, and (iii) how the diffusive GPV fluxes and related processes affect the dynamics of baroclinic wave and associated frontal evolution in terms of GPV thinking. In some aspects, as will be seen, the results obtained in this paper do not agree with the analysis of Cooper et al. (1992). The discrepancies and related problems will be discussed in section 6.

The paper is organized as follows. The model equations and associated GPV equation are presented together with the two types of boundary conditions in the following section. The impacts of different boundary conditions on the initial growths of the viscous Eady waves are examined through linear mode analyses in section 3. Nonlinear solutions are obtained in section 4 where the nonlinear wave structures are examined in association with fronts and frontal circulations for each type of boundary condition. Evolution of GPV anomalies is examined together with GPV fluxes for each type of boundary condition in section 5. Comparisons with Cooper et al. (1992) are made in section 6. The principle results are summarized together with conclusions in section 7.

2. Model equations and boundary conditions

Based on the scale analysis of Xu (1989), we can derive the following viscous SG equations for two-dimensional Eady waves:

$$d_t v_g + fu = Dv, \tag{2.1a}$$

$$d_t b_g + N_o^2 w - f\Lambda v = Db, \tag{2.1b}$$

$$\Lambda w - fv' = Du, \tag{2.1c}$$

$$-b' = Dw, \tag{2.1d}$$

$$\partial_x u + \partial_z w = 0, \tag{2.1e}$$

where $d_t(\,) \equiv [\partial_t + (U + u)\partial_x + w\partial_z](\,)$ is the Lagrangian time derivative, $D = \nu_1\partial_x^2 + \nu_2\partial_z^2$ represents the effect of eddy diffusion with constant coefficients ν_1 and ν_2, $\Lambda \equiv dU/dz =$ constant is the basic flow shear satisfying the thermal wind relationship in association with the meridional gradient of the basic buoyancy (related to the basic potential temperature), N_o^2 is the vertical stratification of the basic buoyancy, (u, w) represents the cross-front ageostrophic wind, v is the along-front wind, $b \equiv g\theta/\theta_o$ is the perturbation buoyancy (related to the perturbation potential temperature), $(v_g, b_g) \equiv (\partial_x\phi/f, \partial_z\phi)$ is the geostrophic part of (v, b) satisfying the thermal wind relationship:

$$f\partial_z v_g = \partial_x b_g = \partial_x\partial_z\phi \equiv S^2, \tag{2.2}$$

ϕ is the perturbation geopotential, and $(v', b') \equiv (v, b) - (v_g, b_g)$ is the ageostrophic part. The ageostrophic part of buoyancy and associated Eq. (2.1d) are similar to those in Xu (1989) but were not considered in Nakamura (1994).

It is necessary to point out that the scale analysis of Xu (1989) does not consider the Ekman layer required by a nonslip boundary condition. With a nonslip boundary condition, the total wind vanishes at the boundary surface, so the horizontal ageostrophic wind approaches the opposite of the geostrophic wind near the surface. In this case, the near-surface geostrophic wind is not small, but its Lagrangian time derivative can be small as long as the near-surface flow field is sufficiently smooth following the streamlines. In this sense, the validity of (2.1a–e) with a nonslip boundary condition can be verified by the streamwise smoothness of the viscous SG Eady wave solution obtained later in this paper. The validity of (2.1a–e) can also be verified numerically by the smallness of the Lagrangian time derivative of the ageostrophic wind in the solution obtained from a prim-

Unauthenticated | Downloaded 08/04/24 02:39 AM UTC

itive equation Eady wave model (not shown but will be reported in a follow-up paper). It is interesting to note that if vertical motion and baroclinicity can be neglected for boundary layer flows (away from a frontal zone), then (2.1a–e) become the two-dimensional version of the upgraded Ekman system of Wu and Blumen (1982). If the Lagrangian time derivative is further neglected, then the system reduces to the classic Ekman system. Like the classic Ekman system, both (2.1a–e) and the upgraded Ekman system of Wu and Blumen (1982) are balanced dynamic systems that filter inertial-gravity waves. The generation of inertial-gravity wave in an unbalanced (primitive equation) Eady wave model will be examined in a follow-up paper.

The GPV, here multiplied by the constant factor of f, can be defined by $q_g \equiv (N_o^2 + N^2 - \Lambda^2)F^2 - S^4$, where $N^2 \equiv \partial_z b_g$ and $F^2 \equiv f(f + \partial_x v_g)$. The GPV equation can be derived from $(N_o^2 + N^2 - \Lambda^2) f\partial_x$(2.1a) $+ F^2\partial_z$(2.1b) $- S^2[f\partial_z$(2.1a) $+ \partial_x$(2.1b)] in the following conservation form:

$$\partial_t q_g + \nabla \cdot (\mathbf{V} q_g + \mathbf{F}) = 0, \tag{2.3}$$

where $\mathbf{V} \equiv (U + u, w)$ is the total cross-frontal velocity in (x, z) space, $\mathbf{V}q_g$ is the advective GPV flux, $\nabla \equiv (\partial_x, \partial_z)$, and $\mathbf{F} \equiv (F_x, F_z) \equiv [S^2 Db - f(N_o^2 + N^2 - \Lambda^2)Dv - \Lambda S^2 Du, fS^2 Dv - F^2 Db + \Lambda F^2 Du]$ is the diffusive GPV flux caused by eddy diffusions of momentum and potential temperature. Since vq_g is uniform in the y direction and the alongfront component of the diffusive GPV flux (if not zero) is also independent of y, the GPV equation can be written into a three-dimensional form by replacing $\nabla \equiv (\partial_x, \partial_z)$ with $\nabla_3 \equiv (\partial_x, \partial_y, \partial_z)$. In its domain-integrated form, the GPV equation reduces to

$$\partial_t\{[q_g]\} = \{F_z\}|_{z=0} - \{F_z\}|_{z=H}, \tag{2.4}$$

where $\{[(\,)]\}$ denotes the domain-integration of $(\,)$ and $\{(\,)\}$ the horizontal integration of $(\,)$. Clearly, (2.4) states that the domain-averaged GPV can be changed only by the diffusive fluxes at the boundaries where the isentropes are terminated, consistent with the theorem due to Haynes and McIntyre (1987). A similar result was obtained by Nakamura (1994) for his viscous SG model.

By substituting (2.1c,d) into $f\partial_z$(2.1a) $- \partial_x$(2.1b) to eliminate (v', b') and using the thermal wind relationship to eliminate the time tendency terms, we can obtain the following extended Sawyer–Eliassen (S–E) equation for the ageostrophic circulation:

$$\partial_x[(D^2 + N_o^2 + N^2 - \Lambda^2)\partial_x\psi] - \partial_z(S^2\partial_x\psi) - \partial_x(S^2\partial_z\psi) + \partial_z[(D^2 + F^2)\partial_z\psi] = 2\Lambda f\partial_x v_g, \tag{2.5}$$

where ψ is the cross-front ageostrophic streamfunction defined by $(-\partial_z\psi, \partial_x\psi) \equiv (u, w)$. Here, (2.5) has the same type of elliptical differential operator as the extended S–E equation previously derived in Xu (1989, 1992) for ageostrophic circulations forced by stretching deformation. According to Xu (1989), the problem of solving for ψ from (2.5) with an appropriate set of boundary conditions is well posed. The existence, uniqueness, and stability of the solution are ensured as long as the geostrophic flow is stable to viscous symmetric perturbations, even when the GPV becomes zero or negative. Mathematically admissible boundary conditions can be derived with proper combinations of boundary-integral terms in the variational formulation [see (A.6) and (A.15) of Xu (1992)]. In this paper, two types of boundary-integral terms are selected (not shown) and the derived admissible boundary conditions have the following forms:

free-slip:

$$\psi = \partial_z^2\psi = L_2\psi + f\partial_z v_g + \Lambda\partial_z\partial_x\psi = 0 \quad \text{at } z = 0, H, \tag{2.6a}$$

nonslip:

$$\psi = \partial_z\psi = fv_g + D\partial_z\psi = 0 \quad \text{at } z = 0, H, \tag{2.6b}$$

where $L_2 \equiv \partial_x D\partial_x + \partial_z D\partial_z$. By using $(u, w) \equiv (-\partial_z\psi, \partial_x\psi)$, $D\partial_z\psi = -Du = fv' - \Lambda w$ [see (2.1c)], $L_2\psi = f\partial_z v' - \partial_x b' - \Lambda\partial_z w$ [obtained from ∂_x(2.1d) $- \partial_z$(2.1c)], and $b' = -Dw = -D\partial_x\psi = 0$ at the free-slip boundaries according to (2.1d), one can verify that (2.6a)–(2.6b) are equivalent to

$$\text{free-slip:} \quad \psi = \partial_z u = \partial_z v = 0 \quad \text{at } z = 0, H, \tag{2.7a}$$

$$\text{nonslip:} \quad \psi = u = v = 0 \quad \text{at } z = 0, H. \tag{2.7b}$$

Note that the above boundary conditions are for the total perturbation flow, so (2.7a) is different from the free-slip boundary condition in (2.8) of Nakamura (1994) as the latter was applied to the ageostrophic flow only. The nonslip boundary condition (2.6b) or (2.7b) has not been previously used for the viscous SG model. Note that the linearly sheared basic flow is precisely maintained through the entire depth by the thermal wind balance in association with the meridional gradient of the basic buoyancy and by the viscous force balance in association with the relative motion of the upper boundary (at the speed of $H\Lambda$) with respect to the lower boundary. This implies that the total perturbation flow should satisfy a homogeneous boundary condition, like the one in (2.7a) or (2.7b). In this sense, the boundary conditions derived here are not only mathematically admissible but also physically acceptable. With (2.6) or (2.7), ψ can be solved diagnostically from (2.5), and then the four ageostrophic components can be obtained from $(u, w) = (-\partial_z\psi, \partial_x\psi)$ and $(v', b') = (\Lambda w - Du, -Dw)$ [see (2.1c,d)].

Since v_g and b_g satisfy the thermal wind relationship, the integration of (2.1a–e) involves essentially only one prognostic variable (ϕ, or one of its derivatives: b_g, v_g, and q_g). The semi-Lagrangian scheme described in appendix B of Xu (1992) is used to integrate (2.1b) for the b_g field with the following thermally insulating boundary condition:

Unauthenticated | Downloaded 08/04/24 02:39 AM UTC

$$\partial_z b_g = 0, \quad \text{at} \quad z = 0, H. \tag{2.8}$$

Here, it is also assumed implicitly that the basic stratification N_o^2 is maintained at the boundaries by some external processes (such as zonal-mean radiative fluxes and surface energy balance). All the perturbation variables are periodic in the x direction with the domain length equal to the wavelength of the unstable linear Eady mode, which is taken to be the initial field. The boundary value problem of (2.5) with (2.6) or (2.7) is solved by using the variational formulation with the finite-element method and cubic-spline basis functions (Xu 1989). One merit of this method is that the boundary conditions that contain high-order derivatives are treated implicitly and all the boundary conditions are satisfied precisely at the boundaries. The computational domain is divided by 85 × 85 subelements. These subelements are nonuniformly distributed in the horizontal with relatively fine resolution (18 km) in the central domain covering the upper and lower frontal regions. Numerical integrations are performed with typical settings of $f = 10^{-4}$ s^{-1}, $\Lambda = 10^{-3}$ s^{-1}, $N_o^2 = 2.5 \times 10^{-5}$ s^{-2}, $H = 10$ km, $\nu_1 = 5 \times 10^4$ m^2 s^{-1}, and $\nu_2 = 5$ m^2 s^{-1}. The basic-state GPV has the value of $q_o = (N_o^2 - \Lambda^2)f^2 = 2.4 \times 10^{-13}$ s^{-4}. The initial b_g field is given by the most unstable linear mode for each type of boundary condition. The linear mode structures and growths are examined in the next section.

3. Linear modes and linear GPV thinking

a. Linearized equations and linear modes

The linearized viscous SG equations have the same forms as (2.1a–e) except that d_t is replaced by $D_t \equiv \partial_t + U\partial_x$ in (2.1a–b):

$$D_t v_g + fu = Dv, \tag{3.1a}$$

$$D_t b_g + N_o^2 w - f\Lambda v = Db. \tag{3.1b}$$

Substituting

$$(u, w, \nu', b', \nu_g, b_g) = (\hat{u}, \hat{w}, \hat{\nu}', \hat{b}', \hat{\nu}_g, \hat{b}_g)e^{ikx+\sigma t} \tag{3.2}$$

into the linearized equations and thermal wind equation (2.2) gives a complete set of ordinary differential equations for $(\hat{u}, \hat{w}, \hat{\nu}', \hat{b}', \hat{\nu}_g, \hat{b}_g)$ in the one-dimensional space of z. The boundary conditions are obtained by substituting (3.2) into (2.7a) or (2.7b). This set of equations poses an eigenvalue problem. For a given wavenumber k, the complex eigenvalue $\sigma = \sigma_r + i\sigma_i$ is computed numerically from the discretized system of the above equations and boundary conditions (with $\Delta z = 0.01H$). The growth rates σ_r are plotted in Fig. 2 for the two types of modes: (i) the unstable mode with the free-slip boundary condition, called the free-slip mode (dashed), and (ii) the unstable mode with the nonslip boundary condition, called the nonslip mode (solid). The growth rate for the inviscid Eady wave mode is also plotted (dotted) for comparison. Clearly, the free-slip mode grows much faster than the nonslip mode, and the growth rate is very close to the inviscid one. Like the inviscid mode, both free-slip and nonslip unstable modes propagate at the same speed as the middle-level basic flow; that is, $-\sigma_i/k = U(H/2)$. The most unstable free-slip and nonslip modes have about the same wavelength of 2000 km (or wavenumber of 3 × 10^{-6} m^{-1}) as the most unstable inviscid mode.

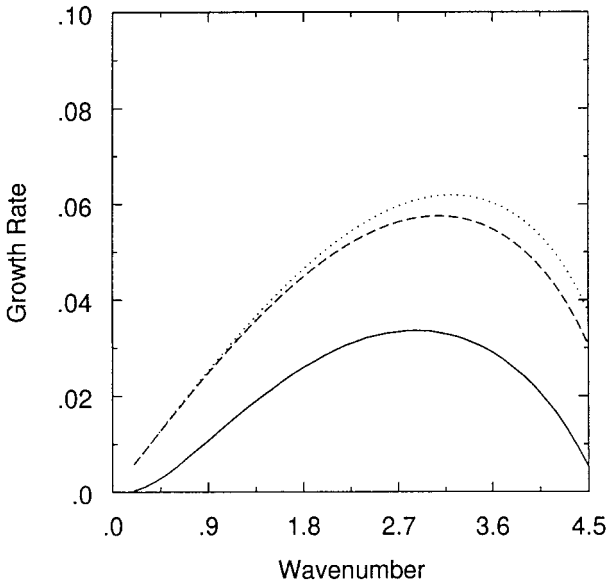

FIG. 2. Growth rates σ_r (10^{-4} s^{-1}) as functions of wavenumber (10^{-6} m^{-1}) for the inviscid Eady wave mode (dotted), free-slip mode (dashed), and nonslip mode (solid). See the end of section 2 for the basic-state parameters.

b. Linearized GPV expression and GPV equation

From the linearized viscous SG equations (3.1a,b) and (2.1c–e), we can derive two forms of GPV equations. The first one maintains the nonlinear GPV expression, $q_g \equiv (N_o^2 + N^2 - \Lambda^2)F^2 - S^4$ as in (2.3), which is derived from $(N_o^2 + N^2 - \Lambda^2)f\partial_x$(3.1a) + $F^2\partial_z$(3.1b) − $S^2[f\partial_z$(3.1a) + ∂_x(3.1b)] in the following conservation form:

$$\partial_t q_g + \nabla \cdot (\mathbf{U}q_g + \mathbf{A} + \mathbf{F}) = 0, \tag{3.3a}$$

where $\mathbf{F}$ is as in (2.3), $\mathbf{U} \equiv (U, 0)$ is the basic flow in (x, z) space, and $\mathbf{A} \equiv (A_x, A_z) = [(N_o^2 + N^2 - \Lambda^2)f^2u - (N_o^2 - \Lambda^2)S^2w, (N_o^2 - \Lambda^2)F^2w - S^2f^2u]$ can be considered as a part of the advective GPV flux in (2.3). Note that $A_z = -S^2f^2u$ at $z = 0$ has the same distribution as $A_z = -S^2f^2u$ at $z = H$ except for a phase shift and change of sign (in u), so $\mathbf{A}$ has no contribution to the domain-averaged GPV and (3.3a) leads to the same domain-averaged formulation as in (2.4). The second GPV equation considers the linearized GPV expression, $q_{lg} \equiv (N_o^2 - \Lambda^2)F^2 + N^2f^2$, which is derived from $(N_o^2 - \Lambda^2)f\partial_x$(3.1a) + $f^2\partial_z$(3.1b) in the following conservation form:

Unauthenticated | Downloaded 08/04/24 02:39 AM UTC

$$\partial_t q_{lg} + \nabla \cdot (\mathbf{U} q_{lg} + \mathbf{F}_l) = 0, \tag{3.3b}$$

where $F_l \equiv [-f(N_o^2 - \Lambda^2)Dv,\ f^2(\Lambda Du - Db)]$ is the linearized diffusive GPV flux. Clearly, (3.3b) can be also obtained by linearizing (3.3a) or (2.3) directly. For a small-amplitude wave, both (3.3a) and (3.3b) are good approximations of (2.3). When the wave amplitude grows to a finite size, (3.3a) may be a slightly better approximation of (2.3) than (3.3b). However, for the linear analyses and GPV thinking developed in the subsequent subsections, (3.3b) is more convenient than (3.3a).

c. Inversion of boundary GPV anomalies—First step of GPV thinking

The linearized GPV anomaly is related to the perturbation geopotential by $q'_{lg} \equiv q_{lg} - q_o = (N_o^2 - \Lambda^2)\partial_x^2\phi + f^2\partial_z^2\phi$. For the inviscid Eady wave mode, there is no interior GPV anomaly, so ϕ is a harmonic function in the space with x scaled by $L = H(N_o^2 - \Lambda^2)^{1/2}/f$ and z by H. The potential temperature anomalies at the two boundaries can be viewed as the surface charges of a problem in electrostatics and the induced geopotential as analogous to the induced electric potential. This analogy makes intuitive the two steps of GPV thinking: (i) inversion of the surface GPV ''charges,'' and (ii) feedback of the inverted geostrophic flow to the growth of the surface GPV ''charges'' [see Eq. (69) of Hoskins et al. 1985]. In the presence of diffusion, interior GPV anomalies are generated by the diffusive GPV fluxes. The potential temperature anomalies at the two boundaries still can be viewed as the surface ''charges,'' but the geostrophic flow field is induced by both the surface and interior ''charges.'' As shown by the linear results in Figs. 3a,b, the interior GPV anomalies are generated mainly within the boundary layers during the initial period, and the depth of the boundary layer is typically $h \approx \pi(2\nu_2/f)^{1/2} \approx 1$ km.

The surface GPV ''charges'' can be expressed as delta-function GPV anomalies at the boundaries, assuming the potential temperature anomalies vanish immediately outside the boundaries (Bretherton 1966). The combined effect of the boundary delta-function GPV anomaly and boundary layer interior GPV anomaly can be measured by the vertical integration of the linearized GPV anomaly $q'_{lg} \equiv q_{lg} - q_o$ through the boundary layer (including the boundary point):

$$\begin{aligned} \mathrm{LPV}(h) &\equiv \int_{0_-}^{h} q'_{lg}\, dz \\ &= (N_o^2 - \Lambda^2)\int_0^h f\partial_x v_g\, dz + f^2 b_g|^{z=h} \\ &\approx f^2 b_g(h), \end{aligned} \tag{3.4a}$$

$$\begin{aligned} \mathrm{UPV}(H - h) &\equiv \int_{H-h}^{H^+} q'_{lg}\, dz \\ &= (N_o^2 - \Lambda^2)\int_{H-h}^{H} f\partial_x v_g\, dz + f^2 b_g|_{z=H-h} \\ &\approx -f^2 b_g(H - h), \end{aligned} \tag{3.4b}$$

where LPV(h) and UPV($H - h$) denote the integrated lower-level and upper-level GPV anomalies, respectively, $b_g(h)$ and $b_g(H - h)$ denote the values of b_g at $z = h$ and $z = H - h$, respectively, and $b_g(0_-) = b_g(H_+) = 0$ are used. The approximation in the last step of (3.4a,b) is actually very accurate according to the following scale analysis:

$$\left[(N_o^2 - \Lambda^2)\int_0^h f\partial_x v_g\, dz\right][f^2 b_g(h)]^{-1} \approx N_o^2 Hh(fL)^{-2} \approx O(10^{-2}), \tag{3.5}$$

where $L = 2\pi/k = 2000$ km is the horizontal wavelength and the thermal wind relationship (2.2) is used. This accuracy is also verified numerically by our linear mode solutions.

Imagine a new boundary at the top of the boundary layer, where the potential temperature anomaly can be viewed as new surface charge. Since interior GPV anomalies can be neglected between the upper and lower imaginary boundaries, the new surface GPV ''charges'' can be inverted as in the inviscid case. This simplifies the first step of GPV thinking. The second step of GPV thinking involves the feedback of the inverted geostrophic flow to the growth of the surface GPV ''charges'' at the imaginary boundaries. The related processes are examined in the next subsection.

d. Growth of boundary GPV anomalies—Second step of GPV thinking

The time evolution of LPV(h) is controlled by the feedback of the inverted geostrophic flow to the growth of the surface GPV ''charges'' at the imaginary boundary $z = h$. The related processes can be analyzed in two steps. First, from (3.1b) and (3.4a) we obtain

$$\begin{aligned} [\partial_t + U(h)\partial_x][\mathrm{LPV}(h)] &\approx f^2 D_t b_g(h) \\ &\approx f^3 \Lambda v_g(h) - f^2 N_o^2 w(h), \end{aligned} \tag{3.6}$$

where $Db(h) \approx 0$ and $v(h) \approx v_g(h)$ are assumed in the last step of (3.6). This result indicates that LPV(h) is produced mainly due to the meridional advection and vertical advection of the basic-state potential temperature. The meridional advection is driven by the geostrophic wind obtained directly from the inversion. The vertical advection, however, is related to the secondary circulation, which is not a direct result of the inversion and requires the following second step of analysis.

Note that

Unauthenticated | Downloaded 08/04/24 02:39 AM UTC

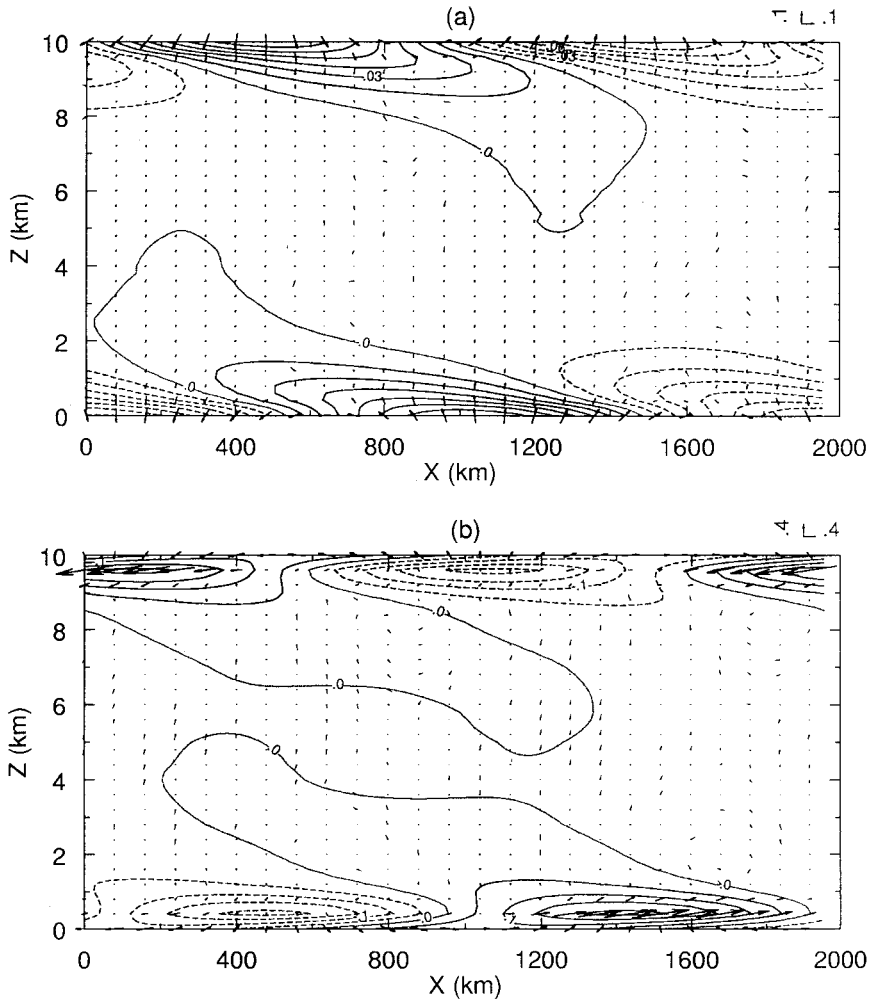

FIG. 3. GPV anomaly field superimposed with diffusive GPV flux for the free-slip mode (a) and nonslip mode (b). The GPV contours (dashed for negative) are every 0.015×10^{-13} s^{-4} in (a) and every 0.05×10^{-13} s^{-4} in (b). The vector scale is $0.1 \times (10^{-13}, 10^{-15})$ m s^{-5} in (a) and $0.4 \times (10^{-13}, 10^{-15})$ m s^{-5} in (b) for the (horizontal, vertical) component of the GPV flux. The amplitude of the mode is specified by $\max(\nu_g) = 1.4$ m s^{-1}. The basic-state GPV has the value of $q_o = (N_o^2 - \Lambda^2)f^2 = 2.4 \times 10^{-13}$ s^{-4}.

$$\mathrm{LPV}(h) = \int_{0_-}^{0} q'_{lg}\, dz + \int_0^h q'_{lg}\, dz = f^2 b_g(0) + \int_0^h q'_{lg}\, dz,$$

so the time evolution of LPV(h) can be evaluated by using (3.1b) and (3.3b):

$$f^2 D_t b_g(0) = f^3 \Lambda v(0) + f^2 Db(0), \tag{3.7a}$$

$$\begin{aligned}\int_0^h D_t q'_{lg}\, dz &= \int_0^h \partial_x [f(N_o^2 - \Lambda^2) Dv]\, dz \\ &\quad - f^2(\Lambda Du - Db)\big|_{z=0}^{z=h} \\ &\approx -f(N_o^2 - \Lambda^2)\partial_x \tau_y(0) - f^3 \Lambda v'(0) \\ &\quad - f^2 Db(0),\end{aligned} \tag{3.7b}$$

where $\tau_y(0) = \nu_2 \partial_z v(0)$ is the meridional wind stress at the surface level. In the last step of (3.7b), (2.8) and (2.1c) with $w(0) = 0$ and $Dv = \nu_2 \partial_z^2 v$ are used, and $Dv(h) \approx 0$ and $Du(h) \approx 0$ are assumed in addition to $Db(h) \approx 0$. The thermal wind relationship (2.2) implies that

$$[(N_o^2 - \Lambda^2) f \partial_x v_g][f^2 \partial_z b_g]^{-1} \approx (N_o H)^2 (fL)^{-2} \ll 1,$$

or

$$O(\varepsilon) \equiv O\{D_t[(N_o^2 - \Lambda^2) f \partial_x v_g]\} \ll O(f^2 D_t \partial_z b_g),$$

so the left-hand side of (3.7b) can be estimated by

$$\int_0^h D_t q'_{lg}\, dz \approx \int_0^h \{f^2 D_t \partial_z b_g\}\, dz + O(\varepsilon h)$$

Unauthenticated | Downloaded 08/04/24 02:39 AM UTC

$$= [\partial_t + U(z)\partial_x](f^2 b_g)|_{z=0}^{z=h} - \int_0^h f^2\Lambda(\partial_x b_g)\,dz + O(\varepsilon h)$$

$$= [\partial_t + U(z)\partial_x](f^2 b_g)|_{z=0}^{z=h} - f^3\Lambda v_g|_{z=0}^{z=h} + O(\varepsilon h).$$

Substituting this estimate into (3.7b) and then combining with (3.7a), we obtain

$$[\partial_t + U(h)\partial_x][\mathrm{LPV}(h)]$$

$$\approx f^3\Lambda v_g(h) - f(N_o^2 - \Lambda^2)\partial_x\tau_y(0) - O(\varepsilon h). \quad (3.8)$$

Comparing (3.8) with (3.6) gives

$$f^2 N_o^2 w(h) \approx f(N_o^2 - \Lambda^2)\partial_x\tau_y(0) + O(\varepsilon h). \quad (3.9)$$

This result shows that the last (vertical advection) term in (3.6) can be related to the curl of the surface wind stress. For the free-slip mode, $\tau_y(0) = \nu_2\partial_z v(0) = 0$ and (3.9) reduces to

$$f^2 N_o^2 w(h) \approx O(\varepsilon h) \quad \text{(for free-slip case)}, \quad (3.10)$$

so $w(h)$ is associated mainly with the frontogenetic process as in the inviscid case. For the nonslip mode, additional vertical motion is generated by the curl of the wind stress through Ekman pumping. The time evolution of UPV($H - h$) can be analyzed similarly. The formulations developed in this and previous subsections will be used to analyze and interpret the numerical results in the next two subsections.

e. GPV anomalies and their interaction in free-slip mode

For the free-slip mode, potential temperature anomalies are maximally produced at the boundaries in the form of delta-function GPV anomalies. The interior GPV anomalies reach maximum values at the boundaries and decrease rapidly away from the boundaries (Fig. 3a). According to (3.4a,b), LPV(z) and UPV($H - z$) approach to their respective boundary GPV anomalies as $z \to 0$, and the variations (from $z = 0$ to $z = h$) manifest the contributions from the boundary layer interior GPV anomalies. The amplitude of LPV(z), scaled by 4.0×LPV(0), and the phase difference, scaled by π, between LPV(z) and UPV($H - z$) are plotted as functions of z in Fig. 4. As shown by the thin dashed curve, the phase lag between UPV($H - z$) and LPV(z) decreases gradually from 0.8π to 0.7π as z increases from 0 to 1 km. This phase lag variation is consistent with the result in Fig. 3a, where the phase lag between the upper- and lower-level interior GPV anomalies is close to a quarter wavelength (0.5π), which is smaller than the phase lag (0.8π) between the upper- and lower-boundary potential temperature anomalies. As shown by the thin solid curve, the amplitude increases only 5% as z increases from 0 to 1 km, so the lower-level and upper-level GPV anomalies are dominated by their respective boundary delta-function GPV anomalies.

Since there is no Ekman pumping effect, the vertical motion is associated mainly with the frontogenetic process as in the inviscid mode. According to (3.6) and (3.10), the surface GPV ''charge'' at the imaginary boundary ($z = h$) is produced nearly in the same way as in the inviscid mode. This explains why the growth rate of the free-slip mode is very close to the inviscid one (Fig. 2). Furthermore, as we have seen from Fig. 4, the surface GPV ''charge'' at $z = h$ is approximately the same as the surface GPV ''charge'' at the real boundary ($z = 0$). The related fact is that the vertical motion is weak at $z = h$ and the surface GPV ''charge'' at $z = h$ is produced mainly by the meridional geostrophic advection of the basic-state potential temperature while the ''charge'' is advected by basic-state zonal flow. The situation is similar to the surface GPV ''charge'' produced at the real boundary. Thus, the growth of the free-slip mode can be interpreted by the interaction between the lower- and upper-surface GPV ''charges,'' at either the two imaginary boundaries or the two real boundaries, through two simple steps of GPV thinking similar to that in the inviscid case.

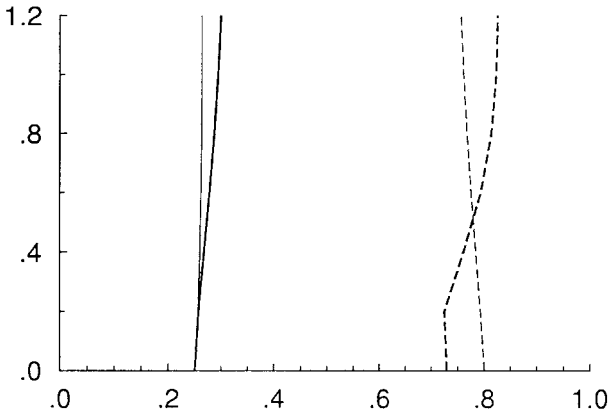

FIG. 4. Phase (dashed) and amplitude (solid) of LPV(z) for the free-slip mode (thin curves) and nonslip mode (thick curves). The phase is scaled by π, and the amplitude is scaled by 4.0 × LPV(0).

f. GPV anomalies and their interaction in nonslip mode

For the nonslip mode, meridional temperature advection vanishes at the boundaries, so boundary potential temperature anomalies are relatively weak as they are produced solely by thermal diffusion from the interior. Interior GPV anomalies produced by the diffusive GPV fluxes are relatively strong in the boundary layers and, as shown in Fig. 3b, the phase lag between the upper- and lower-level interior GPV anomalies is larger than the phase lag (0.72π) between the upper- and lower-boundary potential temperature anomalies. As shown by the thick solid curve in Fig. 4, the amplitude variation of LPV(z) is about 20% of the boundary amplitude, so the boundary layer interior GPV anomalies contribute significantly to the integrated GPV anomalies in (3.4a, b). The boundary layer interior GPV anomalies also

Unauthenticated | Downloaded 08/04/24 02:39 AM UTC

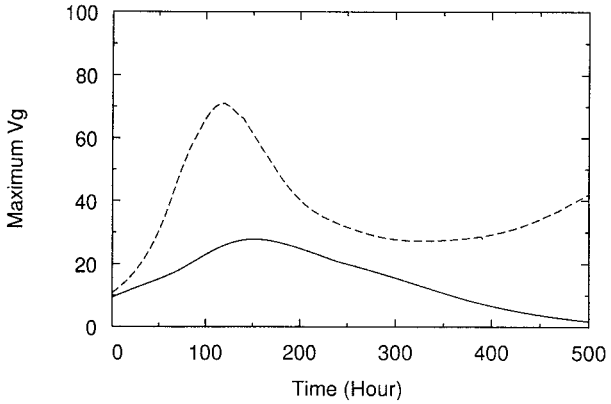

FIG. 5. Time variation of maximum alongfront geostrophic velocity (m s^{-1}) (a) for the free-slip case (dashed) and (b) for the nonslip case (solid).

cause the phase lag to increase from 0.72π to 0.8π, as shown by the thick dashed curve in Fig. 4. This explains why the nonslip mode grows much slower than the free-slip mode.

The growth of the nonslip mode can be interpreted by the interaction between the lower- and upper-surface GPV ''charges'' at the two imaginary boundaries through two steps of GPV thinking. The first step, inversion of the surface GPV ''charges,'' is similar to that in the free-slip mode. The second step, feedback of the inverted flow to the growth of the surface GPV ''charges,'' is complicated by the Ekman pumping [see (3.6) and (3.9)]. As the Ekman pumping produces upward motion at the top of the boundary layer in the warm region where the geostrophic wind shear is cyclonic, the associated adiabatic cooling causes an upstream shift (against the basic flow) of the positive surface GPV ''charge'' (at $z = h$). Thus, in terms of GPV thinking, the primary effect of the surface friction and related Ekman pumping is to increase the phase lag between the upper- and lower-surface GPV ''charges'' at the two imaginary boundaries (Fig. 4). This explains why and how the growth rate of the nonslip mode is reduced by the surface friction through the Ekman pumping. The situation is similar to that of the inviscid mode with an Ekman boundary condition (Blumen 1980).

4. Nonlinear wave solutions and fronts

a. Free-slip case

The free-slip linear mode obtained in the previous section (with wavelength = 2000 km) is used as the initial field for the nonlinear model integration. The maximum alongfront geostrophic velocity is set to 10 m s^{-1} for the initial field. The time evolution of the maximum alongfront geostrophic velocity is shown by the dashed curve in Fig. 5. The initial growth is nearly exponential and closely follows the growth of the linear mode up to $t = 50$ h, then the growth slows down and the wave starts to decay at about $t = 120$ h. Frontogenesis occurs during the development stage, similarly to that in the inviscid case (Hoskins and Bretherton 1972).

The upper and lower fronts are fully developed at $t = 100$ h. As shown for the lower front in Fig. 6, the temperature gradient is very sharp along the frontal zone and the front is steep and extended to the middle layer. The total cross-front flow in Fig. 6 shows that the front acts like a material interface that separates the upward motion ahead of the front from the downward motion behind the front. The alongfront geostrophic velocity has a very sharp cyclonic shear across the front (Fig. 7), indicating that the forcing term in (2.5) is strongly positive and the ageostrophic circulation is strong (close to its maximum intensity). In this case, the adiabatic ascent cooling dominates over the warming caused by the southerly advection in the middle layer ahead of the front, and the adiabatic descent warming dominates over the northerly advective cooling in the middle layer behind the front. This causes, at a later time, the perturbation temperature to change sign in the middle layer, from positive to negative ahead of the front and from negative to positive behind the front (not shown). When the temperature perturbation changes sign in the middle layer, the vertical circulation becomes thermally indirect with cold air rising ahead of the fronts and warm air

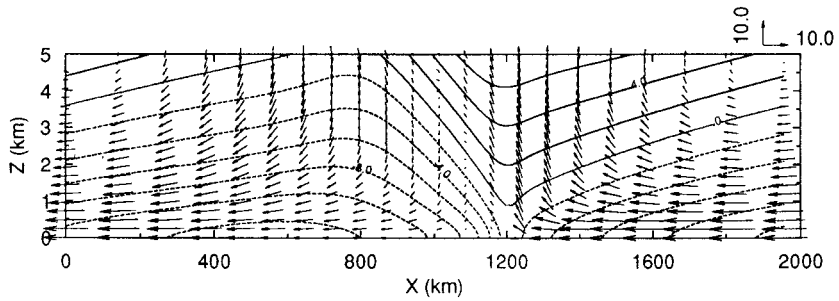

FIG. 6. Potential temperature (N_o^2 z + b_g + b')θ_o/g (contours drawn every 2.0 K with dashed for negative, $\theta_o = 300$ K and $g = 10$ m s^{-2}) and cross-front velocity vectors at $t = 100$ h for the free-slip case. The vector scale for the cross-front velocity is (10, 10^{-1}) m s^{-1} for (horizontal, vertical) component.

Unauthenticated | Downloaded 08/04/24 02:39 AM UTC

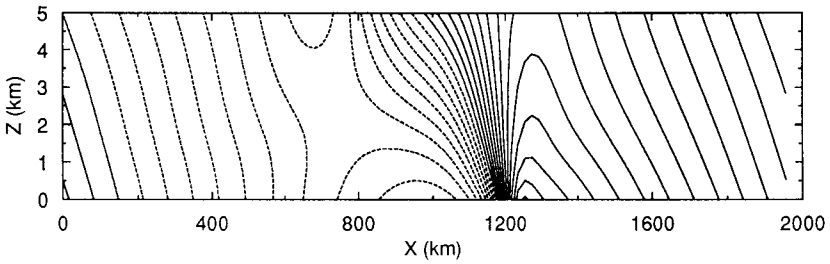

FIG. 7. As in Fig. 6 but for the alongfront geostrophic velocity (contours drawn every 5.0 m s^{-1} with dashed for negative).

sinking behind the front, and the wave starts to decay as shown in Fig. 5. The long-term evolution of the wave is characterized by nonlinear oscillations, similarly to those in Nakamura and Held (1989) and Nakamura (1994).

b. Nonslip case

The nonlinear model integration is initialized by the nonslip linear mode (wavelength of 2000 km) with the maximum alongfront geostrophic velocity set to 10 m s^{-1}. The time variation of the maximum alongfront geostrophic velocity is shown by the solid curve in Fig. 5. The initial growth closely follows the exponential growth of the linear mode up to $t = 50$ h, then the growth slows down and starts to decay at about $t = 160$ h. Since the nonslip boundary condition reduces the alongfront flow and its associated cyclonic shear (not shown), the front is weak and develops slowly. The front becomes matured at $t = 150$ h. At this time, as shown in Fig. 8, the convergence of the horizontal flow is enhanced in the vicinity of the surface front due to the Ekman effect associated with the cross-frontal shear of the alongfront geostrophic flow (Fig. 9). The boundary layer convergence produces a shallow vertical jet immediately ahead of the surface front. Above the boundary layer, the vertical jet turns into a rearward horizontal cross-front flow, and a shallow circulation is formed behind the front where a cold pool is produced by the northerly flow in the boundary layer. The alongfront geostrophic velocity is cyclonically sheared across the front (Fig. 9) but the shear is not as strong as in the free-slip case (see Fig. 7), so the forcing for the ageostrophic circulation in (2.5) is relatively weak.

In the presence of surface friction, the frontal circulation has a complex structure. As shown in Fig. 8, the frontal circulation contains two types of cells: (i) the middle-level cell (between the two boundary layers), which is associated with the dynamic process of frontogenesis; and (ii) the boundary layer cell behind the front, which is driven mainly by the Ekman pumping. In the lower levels, these two cells have their updraft branches jointed into a shallow vertical jet immediately above and ahead of the surface front. This shallow vertical jet is supported mainly by the convergence of boundary layer flow in the vicinity of the front, which locally reinforces the frontogenetic effect. The structure of the flow field in the vicinity of the front is similar to that obtained by Keyser and Anthes (1982) with a primitive equation model. In particular, the solution captures the same three realistic features as in Keyser and Anthes (1982): (i) a narrow updraft at the top of the boundary layer at the warm edge of the frontal zone, (ii) a stable layer capping the boundary layer to the rear of the front zone, and (iii) slightly unstable or neutral lapse rates in the boundary layer behind the front and stable lapse rates in boundary layer ahead of the front. These features remain significant during the decay stage even when the cross-frontal shear of the alongfront geostrophic flow becomes very weak (not shown).

5. Evolution of GPV anomalies and boundary GPV fluxes

a. Free-slip case

As explained in the introduction section, there are two distinctly different stages for the growth of GPV anomalies in the inviscid Eady wave: (i) the boundary stage, and (ii) the interior stage. Two similar stages can be seen for the generation of GPV anomalies in the free-slip case. The boundary stage occurs during the initial period (about 2.5 days) roughly before the surface frontal collapse in the inviscid model. During this stage, GPV anomalies are generated at and near the two boundaries. Near the boundaries, weak GPV anomalies are generated by diffusive GPV fluxes and the situation is similar to that of the linear free-slip mode. At the boundaries, potential temperature anomalies (surface GPV ''charges'') are produced as in the inviscid case. Note that the inviscid linear mode also describes the inviscid nonlinear solution in the SG space (as long as the geostrophic coordinate transformation remains to be a one-to-one mapping), so the two steps of GPV thinking for the linear mode can be directly used for the nonlinear solution in the SG space during the boundary stage. A similar extension can be made for the nonlinear free-slip solution during the boundary stage. By mapping the free-slip solution into the SG space, the wave development can be interpreted by the interaction between

Unauthenticated | Downloaded 08/04/24 02:39 AM UTC

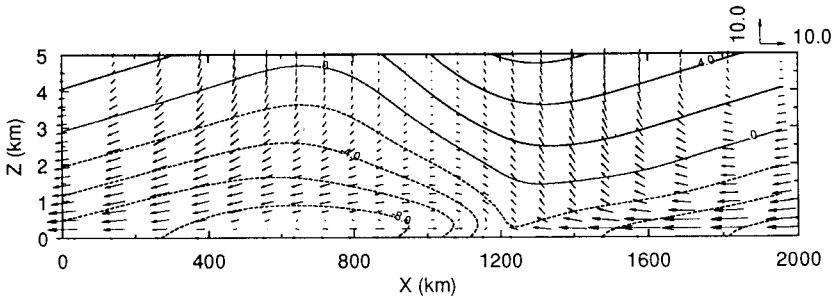

FIG. 8. As in Fig. 6 but for the nonslip case at $t = 150$ h.

the lower- and upper-surface GPV "charges" through the same two steps of GPV thinking as described for the linear free-slip mode in section 3e. The quantitative aspect of this interpretation will be examined in a follow-up paper.

The interior stage occurs after the initial period (after day 2.5). During this stage, strong positive GPV anomalies are produced in the frontal regions by inward diffusive GPV fluxes at the boundaries (Fig. 10a). These GPV anomalies are further advected by the frontal circulation into the interior fluid (Fig. 10b), forming two backward-tilted plumes rooted at the two boundaries (Fig. 11). As the two GPV plumes grow rapidly and become increasingly vertical, their induced geostrophic flow field and associated ageostrophic circulation are contracted horizontally. This in turn causes the two GPV plumes to shift continuously and slowly toward each other in the horizontal direction. When the two GPV plumes collide in the middle layer, they are connected into a single vertical column and start to tilt forward mainly due to the advection of the total cross-frontal flow, which now is dominated by the vertically sheared basic flow. The forward tilted column of GPV anomaly is unfavorable to the wave development and causes the wave and GPV anomalies to decay. By this time, the diffusive GPV fluxes diminish at the boundaries in the vicinities of the two GPV anomaly cores and thus can no longer sustain the positive GPV anomalies. As the two anomaly cores diminish completely (at about $t =$ 320 h), the entire GPV anomaly column is deformed and stretched horizontally by the total flow advection and diluted by the diffusive fluxes. In this case, the zonal-mean state becomes unstable again, and the wave starts to redevelop with two backward-tilted plumes of GPV anomalies regerminated from the two boundaries.

The intrusions of GPV anomalies in the interior stage are related to eddy diffusions of momentum and potential temperature at the surface fronts. The vertical component of the diffusive GPV flux at the lower (or upper) boundary is given by $F_z \equiv fS^2Dv - F^2Db + \Lambda F^2Du$ in (2.3). With the free-slip boundary condition, the leading order terms in the flux formulation can be estimated by

$$F_z \approx fS^2Dv_g - F^2Db_g \approx \nu_1(fS^2\partial_x^2 v_g - F^2\partial_x^2 b_g) \quad \text{at } z = 0, H, \tag{5.1}$$

where the thermal wind relationship is used at the boundary; that is, $f\partial_z^2 v_g = \partial_x\partial_z b_g = \partial_x N^2 = 0$ at $z = 0, H$. Here (5.1) states that the boundary flux F_z is caused mainly by horizontal diffusions of v_g and b_g at the surface frontal region. As shown in Fig. 12a, v_g (solid curve) has a very strong horizontal shear across the surface front and $\nu_1\partial_x^2 v_g$ (dashed curve) is also very strong in the vicinity of the front and changes sign together with fS^2 (dotted curve) across the surface front. Thus, as shown by the solid curve in Fig. 12c, $\nu_1 fS^2\partial_x^2 v_g$ has two peak values: one is ahead of the front and another is behind the front. In Fig. 12b, b_g (solid curve) reaches the peak value immediately ahead of the surface front, $\nu_1\partial_x^2 b_g$ (dashed curve) is negative in a very narrow area ahead of the surface front, and F^2 (dotted curve) is strongly positive in the vicinity of the front. Thus, $-\nu_1 F^2\partial_x^2 b_g$ has a sharp peak value at the surface front as shown by the dashed curve in Fig. 12c. The dotted curve in Fig. 12c is the difference between the flux computed by (5.1) and flux computed by the full

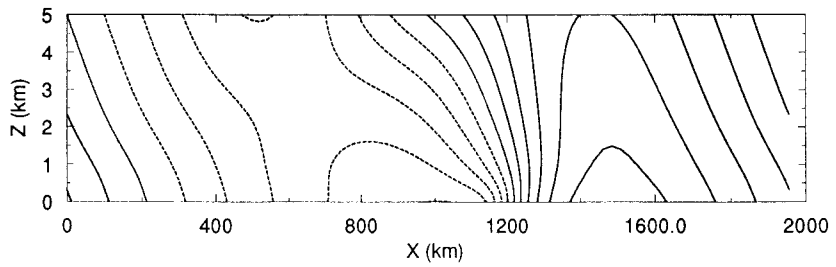

FIG. 9. As in Fig. 7 but for the nonslip case at $t = 150$ h.

Unauthenticated | Downloaded 08/04/24 02:39 AM UTC

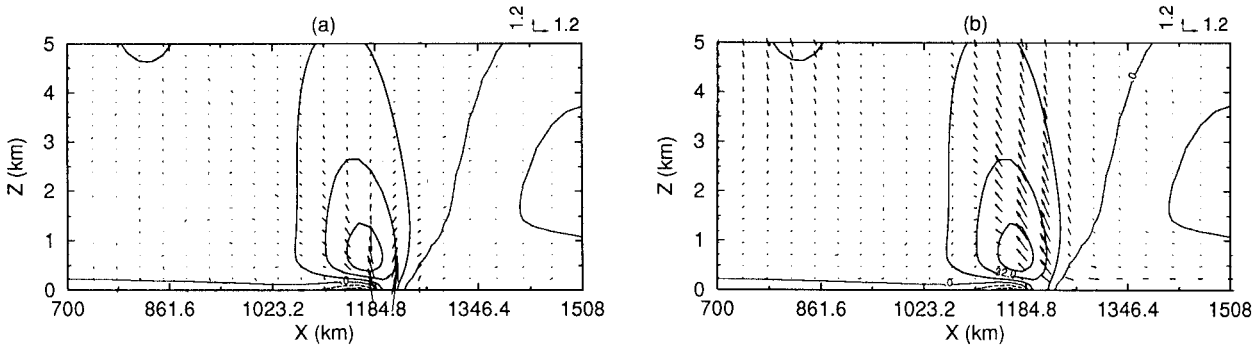

FIG. 10. GPV anomaly field (zoomed in near the surface front) superimposed with diffusive GPV flux (a) and advective GPV flux (b) at $t = 100$ h. The GPV contours are drawn every 1.6×10^{-12} s^{-4}. The vector scale for the GPV flux is $1.2 \times (10^{-11}, 10^{-13})$ m s^{-5} for (horizontal, vertical) component. The basic-state GPV is $q_o = 2.4 \times 10^{-13}$ s^{-4}.

formulation of F_z in (2.3). This difference is much smaller than the major terms in (5.1), so (5.1) is a good approximation.

During the interior stage, the first step of GPV thinking is complicated by the presence of strong positive GPV anomalies in the interior domain and negative GPV in the boundary layers. The negative GPV makes the boundary value problem of inversion locally ill-posed. The problem can be avoided by considering inversion only between the two imaginary boundaries as described in section 3, and the GPV ''charges'' at the imaginary boundaries can be inverted in the SG space similarly to the inviscid case. The two GPV plumes in the interior domain can be viewed as diffused interior delta-function GPV anomalies in the inviscid case (Fig. 1b). In the SG space, the two GPV plumes are transformed into two ''domes'' similar to that in the inviscid case except that the surface GPV ''charges'' mounted on the ''domes'' are now redistributed as GPV ''body charges'' inside the ''domes'' (Purser and Cullen 1987; Koshyk and Cho 1992). These GPV anomalies have the same coarse-grain structure as in the inviscid case, and their inversion is qualitatively similar to that in the inviscid case.

The second step of GPV thinking is also complicated as it involves not only the time evolution of the surface GPV ''charges'' at the two imaginary boundaries but also the time evolution of the interior GPV anomalies. The surface GPV ''charges'' at the imaginary boundaries are produced mainly by the meridional geostrophic advection and vertical ageostrophic advection of the basic-state potential temperature. The generation of the interior GPV anomalies can be viewed as the result of the intrusions of GPV anomalies along the frontal zones from the two imaginary boundaries. The time evolution of the intruded interior GPV anomalies is controlled largely by the geostrophic and ageostrophic advective processes (see Figs. 10a,b), which is qualitatively similar to that in the inviscid case.

b. Nonslip case

In the nonslip case, the boundary stage occurs during the initial period (about 3 days), but there is no clear-cut distinction between this stage and the later interior stage. During the boundary stage, the diffusive GPV fluxes are strong at the two boundaries [see (2.4)], so

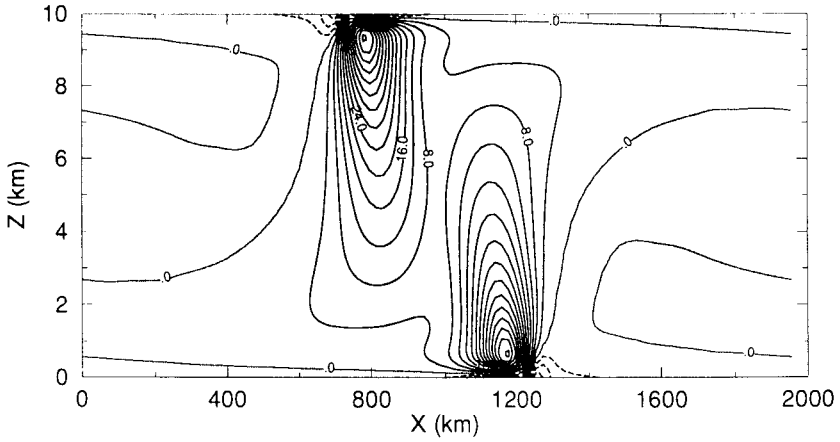

FIG. 11. As in Fig. 6 but for the GPV anomaly field (contours drawn every 4.0×10^{-13} s^{-4} with dashed for negative).

Unauthenticated | Downloaded 08/04/24 02:39 AM UTC

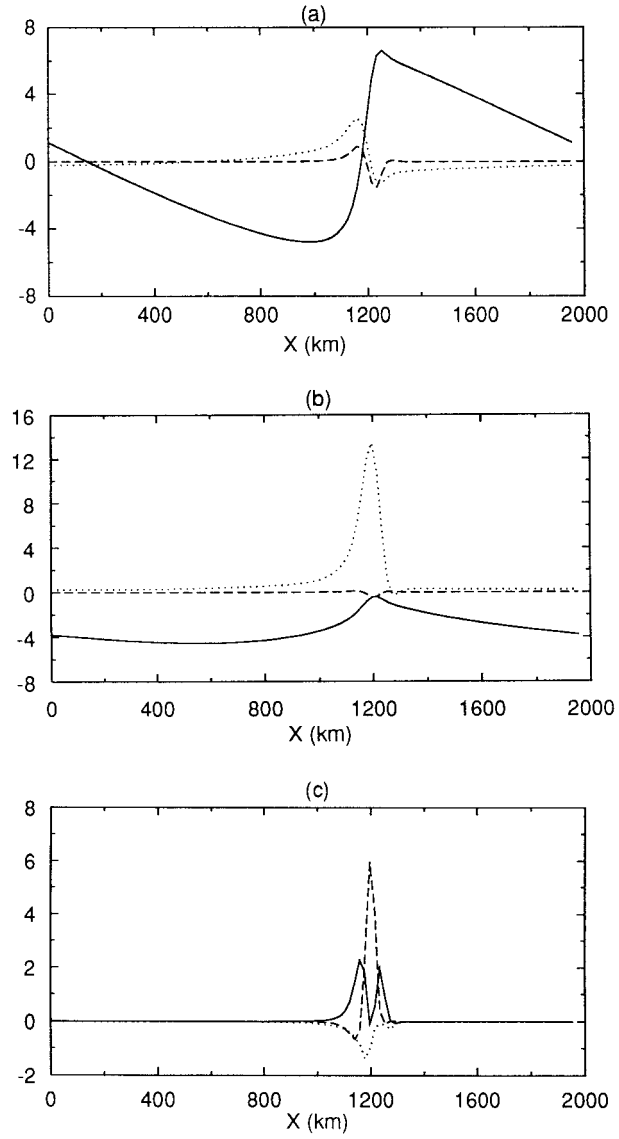

FIG. 12. Horizontal variations of variables in (5.1) along $z = 0$ at $t = 100$ h: (a) ν_g (solid in 10 m s^{-1}), $\nu_1\partial_x^2\nu_g$ (dashed in 10^{-3} m s^{-2}), and fS^2 (dotted in 10^{-10} s^{-3}); (b) b_g (solid in 10^{-1} m s^{-2}), $\nu_1\partial_x^2 b_g$ (dashed in 10^{-5} m s^{-3}), and F^2 (dotted in 10^{-8} s^{-2}); (c) $\nu_1 fS^2\partial_x^2\nu_g$ (solid in 10^{-13} m s^{-5}), $-\nu_1 F^2\partial_x^2 b_g$ (dashed in 10^{-13} m s^{-5}), and the difference (dotted) between the flux computed by (5.1) and flux computed by the full formulation of F_z in (2.3).

GPV anomalies are generated mainly in the two boundary layers and the situation is similar to that of the linear nonslip mode examined in section 3. Loosely, the wave development can be interpreted by the interaction between the lower- and upper-surface GPV ''charges'' at the two imaginary boundaries in the SG space through similar two steps of GPV thinking as described for the linear nonslip mode in section 3f.

As the wave grows continuously, the diffusively generated GPV anomalies are gradually transported farther into the interior domain, so the interior stage occurs gradually. During the interior stage, the diffusive GPV flux is inward at the lower boundary over broad regions behind and ahead of the surface front (Fig. 13a). Behind the front, positive GPV anomalies are transported to a broad region above the boundary layer, the total GPV flux is divergent within the boundary layer, and a negative GPV anomaly is produced locally (Figs. 13a,b). Ahead of the front, the diffusive flux transports positive GPV upward and forward in the lower boundary layer (Fig. 13a), while the cross-frontal circulation advects the GPV anomalies further up, from the top of the boundary layer to a broad interior region (Fig. 13b). Thus, the positive GPV anomalies grow into an upward (downward) mushroom cloud from the lower (upper) boundary (Fig. 14). As the two mushroom clouds grow, they shift slowly and horizontally toward each other. When the two mushroom clouds collide in the middle layer, they form a single column. This column is gradually tilted forward by the total cross-frontal flow advection, whereas the GPV anomalies dissipate continuously. The GPV anomalies nearly diminish after a long time, the zonal-mean state will then become unstable again due to the diffusive process from the boundaries and new GPV anomalies will redevelop. The long-term GPV evolution is beyond the interest of this study.

The generation of GPV anomalies in the interior stage is related to eddy diffusions of momentum and potential temperature at the surface front. With the nonslip boundary condition, the vertical component of the diffusive GPV flux at the lower (or upper) boundary is given by

$$\begin{aligned} F_z &\equiv fS^2Dv - F^2Db + \Lambda F^2Du \\ &= fS^2Dv - F^2Db - \Lambda F^2 f v' \\ &\approx \nu_2(fS^2\partial_z^2 v' - F^2\partial_z^2 b_g) - \Lambda F^2 f v' \quad \text{at } z = 0, H, \end{aligned} \tag{5.2}$$

where $w = 0$ and (2.1c) are used to give $-fv' = Du$ at $z = 0, H$. Here (5.2) states that the boundary flux F_z is caused mainly by vertical diffusions of u, v' and b_g in the boundary layer over the frontal region. As shown in Fig. 15a, v' (solid curve) and $\nu_2\partial_z^2 v'$ (dashed curve) change sign together with fS^2 (dotted curve) across the surface front, so $\nu_2 fS^2\partial_z^2 v'$ (solid in Fig. 15c) has two peak values. In Fig. 15b, b_g (solid curve) and $\nu_2\partial_z^2 b_g$ (dashed curve) reach their maximum values ahead of the front and minimum values behind the front, and F^2 (dotted curve) is strongly positive in the front region. Thus, as shown by the dashed curve in Fig. 15c, $-\nu_2 F^2\partial_z^2 b_g$ is strongly positive behind the front and weakly negative ahead of the front. The distributions of v' (solid in Fig. 15a) and F^2 (dotted in Fig. 15b) suggest that the last term in (5.2) should be positive ahead of the front and negative behind the front, just as shown by the dark-dotted curve in Fig. 15c. The light-dotted curve in Fig. 15c shows that the difference between the flux computed by (5.2) and flux computed by the full

Unauthenticated | Downloaded 08/04/24 02:39 AM UTC

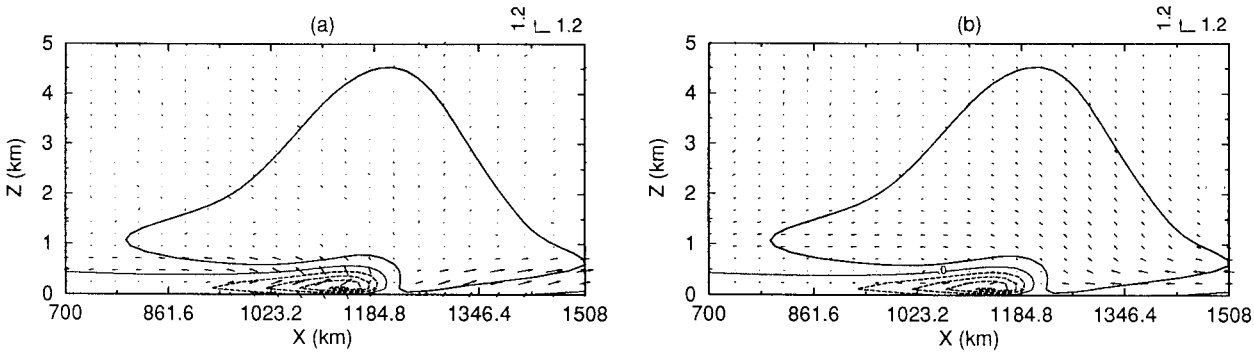

FIG. 13. As in Fig. 10 but for the nonslip case at $t = 150$ h. The GPV contours are drawn every 0.8×10^{-12} s^{-4} (instead of 1.6×10^{-12} s^{-4}).

formulation of F_z in (2.3) is almost zero, so (5.2) is a very good approximation.

During the interior stage, the first step of GPV thinking is complicated by the presence of interior GPV anomalies and negative GPV in the boundary layers. As in the free-slip case, the problem caused by the negative GPV can be avoided by considering inversion between the two imaginary boundaries. The structure of the interior GPV anomalies in the nonslip case, however, is characterized by two mushroom clouds that are relatively flat. Thus, as shown in Figs. 6–9, the inverted geostrophic fields are characterized by relatively strong potential temperature stratification and weak cyclonic wind shear in comparison with those in the free-slip case (Hoskins et al. 1985, 904–905). Because the potential temperature stratification is strong and the geostrophic forcing is weak [see (2.5)], the ageostrophic circulation is weak in the middle levels and the boundary layer circulation produced by the Ekman pumping is shallow as shown in Fig. 8 and discussed in section 4b.

The second step of GPV thinking involves the time evolution of the surface GPV ''charges'' at the two imaginary boundaries and the time evolution of the interior GPV anomalies. The time evolution of the surface GPV ''charges'' at the imaginary boundaries is controlled mainly by the total advection of potential temperature anomalies. The situation is qualitatively similar to that in the boundary stage, except that the vertical motion is further concentrated immediately ahead of the front and, thus, the phase lag between the two positive surface GPV ''charge'' at the upper and lower imaginary boundaries is reduced. The interior GPV anomalies are generated by the diffusive GPV fluxes in the boundary layers and, then, further transported both vertically and horizontally into the interior domain (see Figs. 13a,b). The shallow boundary layer circulation produced by the Ekman pumping is responsible for the horizontal spreading of the GPV anomalies. This explains how this secondary circulation, while driven by the inverted geostrophic flow through the Ekman pumping, produces a positive feedback to the horizontal spreading of the interior GPV anomalies.

6. Comparisons with CTB92

As mentioned in the introduction, a nonslip boundary condition with parameterized turbulent eddy viscosity

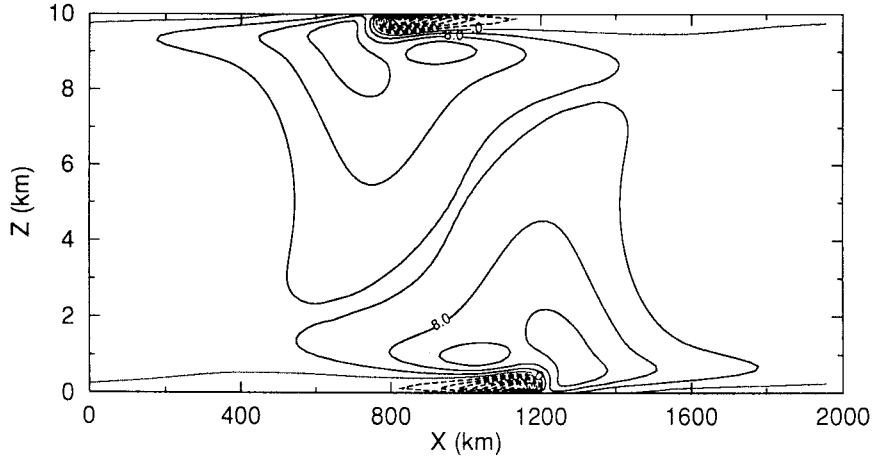

FIG. 14. As in Fig. 11 but for the nonslip case at $t = 150$ h.

Unauthenticated | Downloaded 08/04/24 02:39 AM UTC

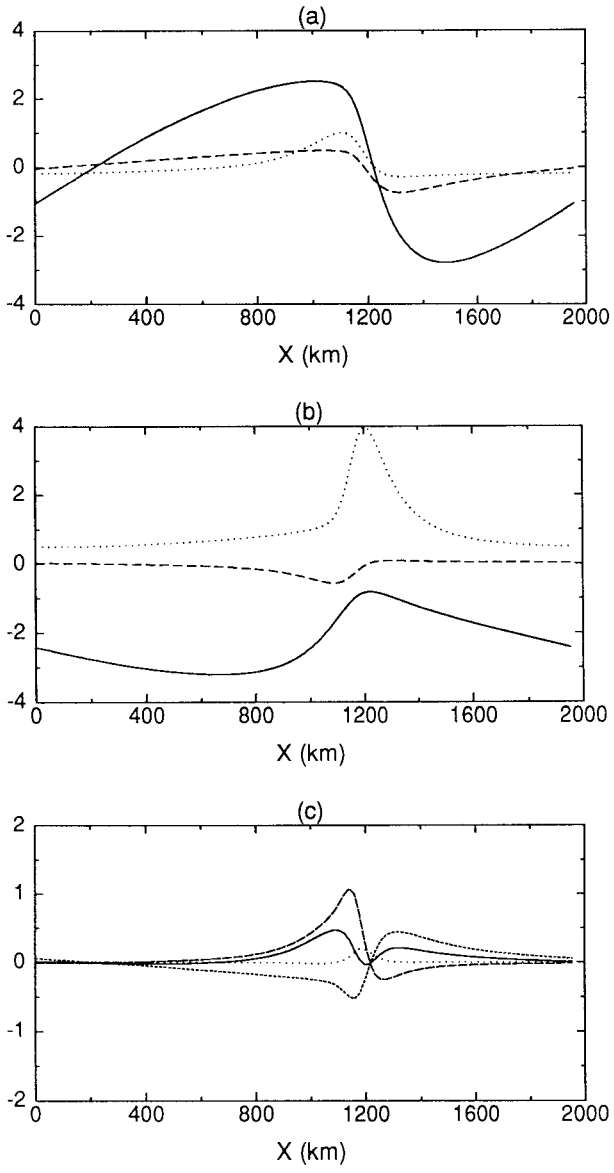

FIG. 15. Horizontal variations of variables in (5.2) along $z = 0$ at $t = 150$ h: (a) v' (solid in 10 m s^{-1}), $\nu_2\partial_z^2 v'$ (dashed in 10^{-3} m s^{-2}), and fS^2 (dotted in 10^{-10} s^{-3}); (b) b_g (solid in 10^{-1} m s^{-2}), $\nu_2\partial_z^2 b_g$ (dashed in 10^{-5} m s^{-3}), and F^2 (dotted in 10^{-8} s^{-2}); (c) $\nu_2 fS^2\partial_z^2 v'$ (solid in 10^{-13} m s^{-5}), $-F^2\nu_2\partial_z^2 b_g$ (dashed in 10^{-13} m s^{-5}), $-\Lambda F^2 f v'$ (dark-dotted in 10^{-13} m s^{-5}), and the difference (light-dotted) between the flux computed by (5.2) and flux computed by the full formulation of F_z in (2.3).

was used by Cooper et al. (1992, referred to as CTB92 hereafter) in their nonhydrostatic model to examine the role of diffusive effects on the Rossby–Ertel potential vorticity (PV) in a two-dimensional Eady wave. Their simulation showed that the low-level PV anomaly was positive ahead of the surface front and negative behind the front during the development stage (day 3, before the occlusion as shown in their Fig. 6a), and this feature is qualitatively similar to that in our nonslip case during the boundary stage (Fig. 3b). However, as the wave further developed and became ''occluded'' (day 5, as shown in their Fig. 6b), the negative PV anomaly behind the surface front changed into a strong positive PV anomaly in their simulation. This rapid change is not seen in the GPV field of our nonslip case. On the contrary, our Fig. 14 shows that the negative GPV anomaly behind the surface front is continuously enhanced as the wave becomes fully developed in the interior stage. This pattern-persistent evolution of GPV anomaly is consistent with the balanced dynamics of our viscous SG model, and the related features are described and explained in terms of GPV fluxes in sections 3 and 5b.

The difference between the Rossby–Ertel PV and GPV may be called ageostrophic PV (APV) and denoted by $q_a = q - q_g$. Since the ageostrophic fields (u, w, v', b') are computed diagnostically in our model, the APV can be estimated. For the nonslip case, $q_a \approx -f^2\Lambda\partial_z\Theta - f\partial_x b\partial_z v'$ is a good approximation for the APV in the boundary layer. For the linear nonslip mode shown in Fig. 3b, we found that $q_a \approx -f^2\Lambda\partial_z v_a - f\partial_x b\partial_z v' < O(10^{-14}\ \text{s}^{-4})$, so the APV is much smaller than the GPV anomalies. When the wave is fully developed (at $t = 150$ h), the APV increases rapidly to $O(10^{-12}\ \text{s}^{-4})$ in the boundary layer behind the surface front, although the increased positive APV (mainly due to $q_a \approx -f\partial_x b\partial_z v'$) does not completely offset the negative GPV anomaly behind the surface front in Fig. 13 [where $\min(q_g) = -2.8 \times 10^{-12}\ \text{s}^{-4}$ and $\max(q_g) = 1.6 \times 10^{-12}\ \text{s}^{-4}$]. The rapid change of the low-level PV (from negative to positive) behind the surface front was not explained in CTB92, but it might be related to nongeostrophic motions. Strictly speaking, it is only the balanced part of the Rossby–Ertel PV, such as GPV, that is invertible and can be used to interpret the dynamics of baroclinic wave and associated frontal evolution in terms of PV thinking (Hoskins et al. 1985). In this sense, the APV is not the active part of PV in our model and, because of this, only the GPV fields are examined in this paper. The GPV field, however, was not examined in CTB92.

By neglecting the horizontal diffusion and integrating the PV equation vertically over the depth of the boundary layer, CTB92 derived an equation for the diffusive generation of PV in the boundary layer. Since the heat flux and wind stress were assumed to decrease linearly with height and become zero at and above the top of the boundary layer, this equation contained only two nonzero diffusive source terms for a nonslip and thermally insulating boundary—that is, terms (b) and (c) in their Eq. (20). Their term (b) was related to the discontinuity of the wind stress force at the top of the boundary layer where the vertical derivative of their assumed wind stress profile jumped from a constant value to zero. This discontinuity implied a delta-function torque in the horizontal (perpendicular to the constant wind stress force in the boundary layer). Thus, their term (b) actually represented the impact (through

Unauthenticated | Downloaded 08/04/24 02:39 AM UTC

the vertical integration) of this delta-function torque multiplied with the horizontal gradient of the potential temperature at the top of the boundary layer. Term (c) in their Eq. (20) was given, with a minus sign, by the vertical average of the vertical torque of viscous force multiplied with the vertical stratification within the boundary layer. These two terms were used in CTB92 to explain the simulated low-level positive PV anomalies behind the surface front (day 5) and ahead of the front (day 3 and day 5) in their Figs. 6a,b. However, closely examining the vertical vorticity fields in their Figs. 5a,b indicates that only term (b) seemed to be a significant positive source of PV, and term (c) was either nearly zero or slightly negative since the vertical vorticity and thus the related torque of viscous force was nearly zero or slightly cyclonic in the concerned regions. Thus, if (20) of CTB92 was a valid approximation, then the above analysis of their results would imply that the low-level positive PV anomalies were generated mainly by the horizontal torque (delta function associated with the jump of the wind stress force) multiplied with the horizontal gradient of the potential temperature at the top of the boundary layer. If this was true, then it would be difficult to explain why the maximum PV anomalies were not generated at the top of the boundary layer but at the surface as shown in Figs. 5a,b of CTB92.

Loosely, (20) of CTB92 can be related to the vertical integration of our GPV Eq. (2.3) through the depth of the boundary layer:

$$D_t \int_0^h q_g \, dz = -\int_0^h \partial_x(uq_g) \, dz - wq_g|^{z=h} - \int_0^h \partial_x(F_x) \, dz - F_z|_{z=0}^{z=h}, \quad (6.1)$$

where $D_t \equiv \partial_t + U\partial_x$, (F_x, F_z) is the diffusive GPV flux vector as in (2.3). Since the first two terms on the right-hand side of (6.1) were not considered in (20) of CTB92, we only need to compare the last two terms in (6.1) with the right-hand side of their (20). Note from (2.3) that $F_x = S^2Db - f(N_o^2 + N^2)Dv + (f\Lambda^2 Dv - \Lambda S^2 Du)$ contains three parts. By substituting this expression into the third term on the right-hand side of (6.1) and using the assumed conditions in CTB92, the first two parts lead to terms (a) and (c) in (20) of CTB92, respectively. The third part is associated with the additional term, $\Lambda^2 f\partial_x v_g$, in the GPV formulation [see the definition of q_g in (2.3)], which is absent in the Rossby–Ertel PV formulation or other balanced PV formulations [see, e.g., (3.4b) of Xu 1994]. Similarly, $F_z = fS^2Dv - F^2Db + \Lambda F^2 Du$ also contains three parts, and the third part is again associated with the additional term, $\Lambda^2 f\partial_x v_g$, in the GPV formulation. Substituting the expression into the last term in (6.1), the first and second parts lead to terms (b) and (d) in (20) of CTB92, respectively. If the wind stress is assumed to decrease linearly to zero at the top of the boundary layer as in CTB92, then the first part of the last term in (6.1) gives $fS^2\nu_2\partial_z^2 v(0) = -fS^2\nu_2\partial_z v(0)/h$, which is essentially the same as term (b) in (20) of CTB92. In general, the wind stress does not decrease linearly in the boundary layer, but often becomes nearly zero above the boundary layer. In this case, $fS^2\nu_2\partial_z^2 v(0)$ remains valid and can be considered as a generalization of term (b) in (20) of CTB92. Note that $fS^2\nu_2\partial_z^2 v(0)$ or term (b) in (20) of CTB92 is a nonlinear term, so it becomes significant only after the wave develops into the nonlinear stage. As shown by (5.2) and Fig. 15c, the second part of the last term in (6.1), $-\nu_2 F^2\partial_z^2 b_g(0)$, also becomes significant and even dominant during the nonlinear stage. This second part corresponds to term (d) in (20) of CTB92, but this term (d) was considered to be small in CTB92.

7. Summary and conclusions

In this paper, the viscous SG model of Xu (1989, 1992) is extended and used to study two-dimensional Eady baroclinic waves with two types of boundary conditions: free-slip and nonslip. Since these two boundary conditions are derived from the variational principle (Xu 1992) and apply to the total perturbation flow, they are mathematically well posed and physically acceptable. The impacts of these boundary conditions on the initial growths of the viscous Eady waves are examined through linear mode analyses. For the free-slip mode, interior GPV anomalies produced by diffusive GPV fluxes near the boundaries are very weak. To the first-order approximation, these interior GPV anomalies can be neglected in comparison with the boundary delta-function GPV anomalies, and this explains why the free-slip mode grows nearly as fast as the inviscid mode. For the nonslip mode, boundary delta-function GPV anomalies are relatively weak as they are produced solely by thermal diffusion from the interior. The primary effect of the surface friction is to produce vertical motion through the Ekman pumping, which increases the phase lag between the delta-function GPV anomalies at the two imaginary boundaries (along the top of each boundary layer). The situation is similar to that of the inviscid mode with an Ekman boundary condition (Blumen 1980), and this explains why the nonslip mode grows significantly slower than the free-slip mode.

Nonlinear solutions are obtained by integrating the viscous SG model initialized by the linear viscous modes. For the free-slip case, the frontogenesis is very similar to the inviscid one. The frontal circulation is strong and the associated adiabatic ascent cooling (or descent warming) dominates over the southerly warm advection (or northerly cold advection) in the middle layer ahead of (or behind) the front. This causes the middle-level temperature anomaly to change sign at a later time, so the frontal circulation will become thermally indirect (with cold air rising ahead of the fronts and warm air sinking behind the front). However, before this occurs, the zonal-mean stratification is enhanced by

Unauthenticated | Downloaded 08/04/24 02:39 AM UTC

the thermally direct circulation. The nonlinear wave also produces a supergeostrophic shear (not shown) in the zonal-mean flow that stabilizes the flow and causes the wave to decay rapidly due to the mechanism explained by Nakamura (1994).

The nonslip boundary condition reduces the along-front flow and its associated cyclonic shear, so the front is relatively weak and develops slowly. The frontal circulation contains two types of cells: (i) the middle-level cell associated with the dynamic process of frontogenesis, and (ii) the shallow boundary layer cell behind the front driven mainly by the Ekman pumping. The gross structure of the flow field in the vicinity of the front is similar to that obtained by Keyser and Anthes (1982) with a primitive equation model. As in Keyser and Anthes (1982), the nonslip solution captures several realistic features (see section 4b) that are not seen in the free-slip case. The nonlinear wave produces a supergeostrophic shear in the middle layer but the shear is much weaker than that in the free-slip case.

The domain-averaged GPV can be changed only by the diffusive fluxes at the boundaries [see (2.3)–(2.4)]. In the free-slip case, prior to the intrusion of GPV anomalies into the interior fluid, weak GPV anomalies are produced by diffusive GPV fluxes near the boundaries, whereas strong delta-function GPV anomalies are generated by meridional temperature advection at the boundaries. As the front becomes sharp, inward GPV fluxes are enhanced dramatically at the boundaries due to the increased horizontal diffusions of momentum and potential temperature at the fronts, so high GPV anomalies are generated at the surface fronts and advected into the interior fluid, forming two backward-tilted plumes (Fig. 11). These two stages of GPV anomaly generation are qualitatively similar to those in the inviscid Eady wave (Fig. 1), although they are affected by the diffusive GPV fluxes. The wave and front development can be interpreted by the interaction between the lower- and upper-level GPV anomalies through two steps of GPV thinking similarly to that in the inviscid case (see section 5a).

The generation of GPV anomalies in the nonslip case can be also viewed in two stages, although there is no clear-cut distinction between the two stages. In the boundary stage, relatively strong GPV anomalies are produced by diffusive GPV fluxes in the boundary layers, and the delta-function GPV anomalies are weak due to vanished meridional temperature advection at the boundaries. In the interior stage, positive GPV anomalies are produced by inward GPV fluxes over broad regions (behind and ahead of the fronts) and advected into the interior region. Since the inward GPV fluxes are caused mainly by the vertical diffusions (instead of horizontal diffusions) of momentum and potential temperature at the nonslip boundaries, the structure and time evolution of GPV anomalies are very different from those in the free-slip case. As the shallow boundary layer circulation is driven by the inverted geostrophic flow through Ekman pumping, it produces a positive feedback to the horizontal spreading of the interior GPV anomalies. This explains in terms of GPV thinking why and how the GPV anomalies grow into two mushroom clouds (Fig. 14).

Acknowledgments. We are thankful to the anonymous reviewers for their comments that improved the presentation of the results. The numerical experiments were performed on the Cray-C90 at the Pittsburgh Supercomputing Center (PSC), and on the Cray-J90 of the Environmental Computing Applications System (ECAS), University of Oklahoma. Figures are produced by using the ZXPLOT graphic package written by Dr. Ming Xue. This work was supported by the NSF Grant ATM-9417304 and NOAA Grant NA67RJ0150 to CIMMS and NSF Grant ATM91-20009 to CAPS at the University of Oklahoma and by the Office of Naval Research (ONR), Program Elements PE602435N and PE601153N to the Marine Meteorology Division of the Naval Research Laboratory at Monterey.

REFERENCES

Blumen, W., 1980: A comparison between the Hoskins-Bretherton model of frontogenesis and the analysis of an intense surface frontal zone. *J. Atmos. Sci.,* **37,** 64–77.

Bretherton, F. P., 1966: Critical layer instability in baroclinic flows. *Quart. J. Roy. Meteor. Soc.,* **92,** 335–345.

Cho, H.-R., and J. N. Koshyk, 1989: Dynamics of frontal discontinuities in the semigeostrophic theory. *J. Atmos. Sci.,* **46,** 2166–2177.

Cooper, I. M., A. J. Thorpe, and C. H. Bishop, 1992: The role of diffusive effects on potential vorticity in fronts. *Quart. J. Roy. Meteor. Soc.,* **118,** 629–647.

Cullen, M. J. P., and R. J. Purser, 1984: An extended Lagrangian theory of semigeostrophic frontogenesis. *J. Atmos. Sci.,* **41,** 1477–1497.

Garner, S. T., I. M. Held, and N. Nakamura, 1992: Nonlinear equilibration of two-dimensional Eady waves: A new perspective. *J. Atmos. Sci.,* **49,** 1984–1996.

Haynes, P. H., and M. E. McIntyre, 1987: On the evolution of vorticity and potential vorticity in the presence of diabatic heating and friction or other forces. *J. Atmos. Sci.,* **44,** 828–841.

Hoskins, B. J., 1975: The geostrophic momentum approximation and the semigeostrophic equations. *J. Atmos. Sci.,* **32,** 233–242.

——, and F. P. Bretherton, 1972: Atmospheric frontogenesis models: Mathematical formulation and solution. *J. Atmos. Sci.,* **29,** 11–37.

——, M. E. McIntyre, and A. W. Robertson, 1985: On the use and significance of isentropic potential vorticity maps. *Quart. J. Roy. Meteor. Soc.,* **111,** 877–946.

Keyser, D., and R. A. Anthes, 1982: The influence of planetary boundary layer physics on frontal structure in the Hoskins-Bretherton deformation model. *J. Atmos. Sci.,* **39,** 1783–1802.

Koshyk, J. N., and H.-R. Cho, 1992: Dynamics of mature front in a uniform potential vorticity semigeostrophic model. *J. Atmos. Sci.,* **49,** 497–510.

Nakamura, N., 1994: Nonlinear equilibration of two-dimensional Eady waves: Simulations with viscous geostrophic momentum equations. *J. Atmos. Sci.,* **51,** 1023–1035.

——, and I. M. Held, 1989: Nonlinear equilibration of two-dimensional Eady waves. *J. Atmos. Sci.,* **46,** 3055–3064.

Purser, R. J., and M. J. P. Cullen, 1987: A duality principle in semigeostrophic theory. *J. Atmos. Sci.,* **44,** 3449–3468.

Unauthenticated | Downloaded 08/04/24 02:39 AM UTC

Wu, R., and W. Blumen, 1982: An analysis of Ekman boundary layer dynamics incorporating the geostrophic momentum approximation. *J. Atmos. Sci.,* **39,** 1774–1782.

Xu, Q., 1988: Baroclinic waves and frontogenesis with an embedded zone of small moist symmetric stability. *Quart. J. Roy. Meteor. Soc.,* **114,** 1221–1251.

——, 1989: Extended Sawyer–Eliassen equation for frontal circulations in the presence of small viscous moist symmetric stability. *J. Atmos. Sci.,* **46,** 2671–2683.

——, 1990: Cold and warm frontal circulations in an idealized moist semigeostrophic baroclinic wave. *J. Atmos. Sci.,* **47,** 2337–2352.

——, 1992: Formation and evolution of frontal rainbands and geostrophic potential vorticity anomalies. *J. Atmos. Sci.,* **49,** 629–648.

——, 1994: Semi-balance model—Connection between geostrophic-type and balanced-type intermediate models. *J. Atmos. Sci.,* **51,** 953–970.

Unauthenticated | Downloaded 08/04/24 02:39 AM UTC